

Article

Not peer-reviewed version

A Device-on-Chip Solution for Real-Time Diffuse Correlation Spectroscopy Using FPGA

Christopher Moore , [Ulas Sunar](#) , [Wei Lin](#) *

Posted Date: 1 May 2024

doi: 10.20944/preprints202405.0056.v1

Keywords: diffuse correlation spectroscopy; FPGA; device-on-chip; FPGA correlator



Preprints.org is a free multidiscipline platform providing preprint service that is dedicated to making early versions of research outputs permanently available and citable. Preprints posted at Preprints.org appear in Web of Science, Crossref, Google Scholar, Scilit, Europe PMC.

Copyright: This is an open access article distributed under the Creative Commons Attribution License which permits unrestricted use, distribution, and reproduction in any medium, provided the original work is properly cited.

Article

A Device-on-Chip Solution for Real-Time Diffuse Correlation Spectroscopy Using FPGA

Christopher Moore, Ulas Sunar and Wei Lin *

Department of Biomedical Engineering, Stony Brook University, Stony Brook, NY 11794, USA; christopher.h.moore@stonybrook.edu (C.M.); ulas.sunar@stonybrook.edu (U.S.)

* Correspondence: wei.lin@stonybrook.edu

Abstract: Diffuse correlation spectroscopy (DCS) is a non-invasive technology for the evaluation of the blood perfusion in deep tissue. However, it requires high computational resources for data analysis which poses challenges in its implementation for real-time applications. To address the unmet need, we developed a novel device-on-chip solution that fully integrates all the necessary computational components needed for DCS. It takes the output of a photon detector and determines the blood flow index (BFI). It is implemented on a Field Programmable Gate Array (FPGA) chip including a multi-tau correlator for the calculation of the temporal light intensity autocorrelation function and a DCS analyzer to perform the curve fitting operation that derives the BFI. The FPGA DCS system was evaluated against a lab-standard DCS system for both phantom and cuff-ischemia studies. The results indicate that the autocorrelation of the light correlation and BFI from both the FPGA DCS and the reference DCS matched well. Furthermore, the FPGA DCS system was able to achieve a measurement rate of 50 Hz and resolve pulsatile blood flow.

Keywords: diffuse correlation spectroscopy; FPGA; device-on-chip; FPGA correlator

1. Introduction

Diffuse correlation spectroscopy (DCS) is an optical technique for non-invasively monitoring the blood perfusion in microvasculature using the blood flow index (BFI) derived from the autocorrelation model of scattered light from moving blood cells, as detailed in previous reviews [1–6]. It has previously been shown that DCS measurements correlate well with established modalities such as arterial-spin labelled magnetic resonance imaging (ASL-MRI) [7–10] and Doppler ultrasound [3,11–16], with its advantages that DCS has a lower cost and more portability than MRI and more sensitivity to microvasculature than Doppler ultrasound. Thus, DCS has found numerous applications related to bedside monitoring of several disease conditions including acute brain injuries [1,17–28] and monitoring of cancer therapies [1–6,29–38].

A typical DCS system is composed of an optical component and an electronic component. The optical components consist of a multi-mode source fiber coupled to a high-coherence laser and a single-mode detector fiber coupled to an avalanche photodiode (APD). When the laser fiber illuminates the tissue, the intensity of the scattered light is monitored by the APD through the detector fiber. Each pulse from the electrical output of the APD corresponds to a single captured photon. The movement of scatterers in the tissue, primarily red blood cells, causes fluctuations in the intensity over time that can be quantified with a temporal intensity autocorrelation function. The decay of the correlation is related to the motion of the light scatterers. Fast-moving scatterers cause more rapid changes in the scattered light; therefore, faster decays in the correlation indicate faster motion [1–6,39,40]. A diffusion correlation equation relates the rate of decay of the correlation to the BFI [1–6]. Therefore, by fitting this model equation to the measured correlation, the BFI can be quantified.

The electronic component of DCS has three major features: counting the number of photons in a predefined time bin, calculating the autocorrelation of the photon counts, and fitting the measured

correlation to the diffusion correlation equation to derive the BFI. The correlation and fitting are both computationally intensive tasks. For the correlation calculation, most DCS systems employ either a counter acquisition board that counts output pulses from the detector connected to a computer with a software correlator [41–43] or a commercial hardware correlator board that performs both functions [1–6]. Each of these configurations comes with limitations. Software correlators are flexible and can be configured to only calculate physiologically relevant correlations for predetermined delay times, but they require high-performance computers to perform the calculations, which can take long time to complete especially for the high frame rate of DCS data acquisitions. Moreover, in neurointensive care units, clinicians are interested in having real-time BFI as an additional local cerebral health metric as an adjunct to other standard clinical monitoring parameters such as mean arterial pressure (MAP), heart rate (HR), oxygen saturation (SpO₂), intracranial pressure (ICP), etc. Commercial hardware correlators are more powerful as they are based on field-programmable gate arrays (FPGA) that can perform the calculations in real-time. However, they are less flexible and hard for end users to reconfigure. Several custom, open-source FPGA correlator designs have been made that provide much greater flexibility, but they have not yet been applied to DCS applications [44–49].

The BFI is obtained by fitting a theoretical diffusion correlation equation with the acquired correlation values. The curve fitting can be performed with a least-squares criterium. The residual sum of squares between the theoretical equation and the acquired correlation is calculated and then minimized using algorithms like the Nelder-Mead method [50]. The fit is nonlinear and computationally intensive. Currently, curve fitting for DCS is mostly performed in software. As a result, these fits are difficult to do in real time and are often done in post-processing [45,51]. Therefore, it is difficult to perform real-time DCS measurements, especially with multiple DCS channels running at a fast measurement rate without a high-performance computer. Lin et al. [45] developed a DCS analyzer that successfully implemented the curve fitting algorithm with the Nelder-Mead method on FPGA. The design was made using LabVIEW FPGA development tools and tested on a National Instruments FPGA module. It was shown to be able to achieve a processing speed of less than 1 ms per fit. This demonstrated the potential for offloading DCS data processing to an FPGA and the development of a portable DCS system.

The objective of this work is to develop a single-chip solution for the electronic components of the DCS system. It integrates our previous work of an open-source FPGA correlator with our new FPGA DCS analyzer module to determine the BFI. It includes a photon counter, a hardware correlator, a DCS analyzer, and a system control microcontroller, which are all implemented on one FPGA chip using the Very High Speed Integrated Circuit Hardware Description Language (VHDL). The design is universal and can be implemented on any FPGA chip with sufficient resources. The DCS system presented here significantly reduces the computational hardware needed for DCS and easily allows for real-time processing at high measurement rates.

2. Materials and Methods

Our DCS system is composed of several high-level components integrated on our FPGA. First, a photon counting module takes the direct electrical output from the APD to determine the photon counts within a preset time bin. Second, the binned counts are passed to a correlator module to generate the autocorrelation of the light intensity. Finally, a DCS analyzer module performs the curve fitting process to extract the final BFI result. The operation of these modules is controlled by a Microblaze soft microprocessor core.

2.1. DCS Analyzer Module

The DCS analyzer for our system is based on the architecture of the analyzer previously presented by Lin et al. [45]. We follow the same principle of curve fitting by minimizing the residual sum of squares between the measured autocorrelation and the correlation of the theoretical model. The minimization is performed using the Nelder-Mead method, which is an iterative algorithm for minimization without the calculation of gradients [50]. The basis for this algorithm is performing operations on a simplex to efficiently converge to the solution that minimizes the function. The

operations allow the simplex to explore the search space for the minimum of the function through geometric reflections, contractions, expansions, and shrinks. The DCS analyzer used the correlation diffusion equation for semi-infinite diffuse medium model [1–6], where αD_B is equivalent to BFI. The simplified version of the equation can be represented as shown previously by Lin et al. [45]. This leaves two free parameters to fit, the αD_B (BFI) and β . Thus, we are working with a two-dimensional space and our simplex is a triangle. The αD_B and β values represent the x and y coordinates for each vertex of the triangle.

$$g_2 = 1 + \beta \left(\frac{e^{-r_1 \sqrt{A+B\alpha D_B \tau}}}{r_1 H} - \frac{e^{-r_b \sqrt{A+B\alpha D_B \tau}}}{r_b H} \right)^2 \quad (1)$$

where:

$$\begin{aligned} A &= 3\mu'_s \mu_a \\ B &= 6(\mu'_s)^2 \kappa_0^2 \\ r_1 &= \sqrt{\left(\frac{1}{\mu'_s}\right)^2 + \rho^2} \\ r_b &= \sqrt{\left(2z_b + \frac{1}{\mu'_s}\right)^2 + \rho^2} \\ H &= \left(\frac{e^{-r_1 \sqrt{A}}}{r_1} - \frac{e^{-r_b \sqrt{A}}}{r_b} \right) \\ z_b &= \frac{2}{\mu'_s} \frac{1 + R_{eff}}{3(1 - R_{eff})} \end{aligned}$$

Equation 1. The semi-infinite solution to the correlation diffusion equation. A, B, H, r_1 , and r_b are fixed parameters derived from μ'_s , the reduced scattering coefficient, μ_a , the absorption coefficient, κ_0 , the wave number, ρ , the source-detector separation, and R_{eff} , the effective Fresnel reflection coefficient. The free parameters that are fit by the analyzer are αD_B and β .

The DCS analyzer uses a central state machine along with several submodules to perform the curve fitting operation with the Nelder-Mead method as shown in Figure 1. The equation constants are stored in registers and the measured correlation along with the associated time delays are stored in memory prior to the fitting process for later use. When starting the analyzer, the state machine takes an initial simplex formed by three pairs of β and αD_B then passes them to the mean squared error (MSE) pipeline module. The MSE pipeline takes a β - αD_B coordinate pair and calculates the theoretical correlation given by the semi-infinite model in Equation 1. It receives the constants used in the equation from the state machine then determines the MSE between the calculated theoretical correlation and the measured correlation. The three β - αD_B pairs and their corresponding MSE values are then sorted by the sorter module to find the best, good, and worst point, which correspond to the lowest, middle, and highest MSEs respectively. This initial simplex is then sent to the point calculator module. This module calculates new β - αD_B pairs for the reflected, contracted, expanded, and shrunk locations according to the rules defined in the Nelder-Mead method. The β - αD_B pairs are then passed in the above order to the MSE pipeline module to determine their MSE values for the decision maker module to find the best β - αD_B pair that should be used to replace the previous worst pair in the simplex.

The decision-maker module determines the best β - αD_B choice following the rules outlined by the Nelder-Mead method [50,52]. It may find the β - αD_B pair before the MSE values of all the new β - αD_B pairs are determined. At this point, the MSE pipeline is cleared so that the next iteration of the Nelder-Mead method can start early. The termination module then checks if convergence has been

reached. The conditions for termination of the search are either the percent difference between the best and worst points in the Nelder-Mead simplex being less than the preset threshold or exceeding the maximum number of allowed iterations of the algorithm. If the convergence is not met, the iteration will start on the newly generated simplex.

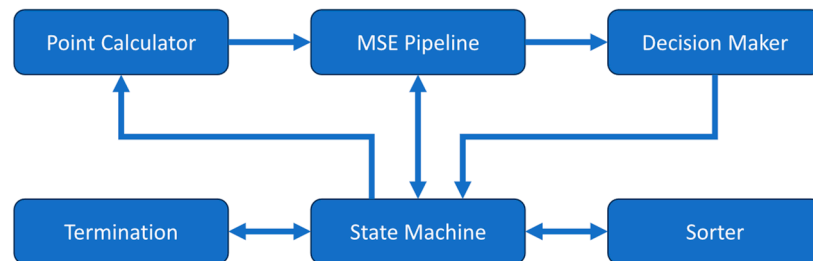


Figure 1. Block diagram of submodules making up the DCS analyzer module. A central state machine controls the operation and flow of data between the other submodules.

2.2. Autocorrelator Module

The correlator used for this DCS system is a flexible hardware FPGA correlator we previously described [44]. This correlator was designed to be very flexible, allowing for numerous configurations of the calculated delays and the choice between auto- and cross-correlation. For our application, we configured our correlator to calculate the autocorrelation function. We also use a multi-tau scheme that calculates the correlation for a quasi-logarithmic scale of delays. We made two different correlator delay configurations for use with two experiments. One configuration calculated 80 total delays for use with physiological measurements and liquid phantoms while the other calculated 120 delays for use with solid phantoms to capture the slow decay. Both configurations use a 16-delay first stage followed by the appropriate number of multi-tau stages, each calculating 8 delays. Only one of these correlator configurations is implemented in the FPGA at a time.

2.3. Full DCS System Integration

The optical components used for our DCS system are standard for continuous wave (CW) DCS. The light source is from a long coherence length, 785nm continuous laser (DL785-100, CrystaLaser Inc., Reno, NV) coupled to a 600 μm multi-mode fiber. The 5 μm single-mode detector fiber is coupled to an APD (SPCM-780-12-FC, Waltham, MA).

The APD output is a series of approximately 2V pulses and requires a 50 Ω load. We used the Arty A7-100T FPGA development board (Digilent, Inc., Pullman, WA) for this project. The board hosts a Xilinx Artix-7 FPGA (XC7A100TCSG324-1, AMD, Santa Clara, CA), which has 101k logic cells, 240 DSP units, and 4860 kbits of block memory. The evaluation board provides Pmod connectors that allow for I/O to the FPGA. Since the I/O pins for the FPGA are configured to use 3.3V LVCMOS logic levels and do not have the proper 50 Ω impedance, an interface board was built to bring the APD pulse into the FPGA. We built a custom-printed circuit board to provide the interface between the BNC output of the detector and the Pmod port on the FPGA as shown in Figure 2. It provides the necessary termination resistor for the APD output and performs a logic level shift to raise the voltage to the 3.3V LVCMOS logic level usable by the FPGA.

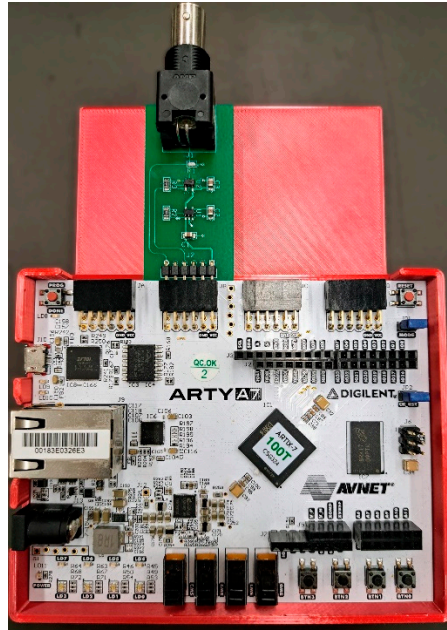


Figure 2. Arty A7 FPGA development board and the custom interface board connected to a Pmod port.

The overall design of the DCS processing system is shown as a block diagram in Figure 3. All modules run at a frequency of 100MHz. A MicroBlaze softcore microprocessor Xilinx IP (Xilinx, Inc., San Jose, CA) is used as the system controller. Its primary function is to control the flow of data through the correlator and analyzer. The MicroBlaze IP is configured as a 32-bit processor with a five-stage pipeline, basic floating-point unit, and 32kB of on-chip block RAM. It also has an interrupt controller supporting fast interrupts to reduce latency during interrupt handling. It has an AXI4-Lite interface available for peripheral connections.

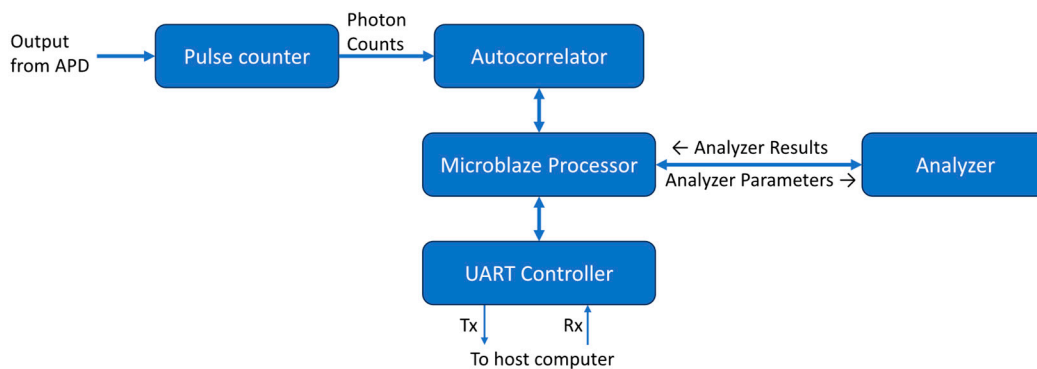


Figure 3. Block diagram showing major FPGA modules used for the full DCS processing system. Single-headed arrows represent unidirectional data flow while double-headed arrows represent bidirectional data flow. A Microblaze soft microprocessor core is used to integrate the different components making up the system.

The photon counter module counts pulses from the APD within a time bin of a predetermined duration. The time bin used by our system was $1\mu\text{s}$ and is controlled by a dedicated timer. When the timer times out at $1\mu\text{s}$, the module outputs the counter value and resets it for the next $1\mu\text{s}$ time bin. The binned counts from the pulse counter module are then passed to the previously described autocorrelator module to calculate the intensity autocorrelation.

The measured correlation from the correlator is written into a dual-port block RAM. One port is used by the correlator to write the correlation and the other is used by the MicroBlaze processor to

read from the memory. The flag signal of the last data output from the correlator is used as an interrupt to inform the MicroBlaze processor that new correlation data is ready for processing. The processor performs basic checks on the correlation data. It ensures that the first and last data points of the autocorrelation are within the expected range. If the autocorrelation passes the check, it will be sent to the DCS analyzer along with the necessary correlation model parameters. The analyzer issues an interrupt to inform the processor when curve fitting is complete and that the results are available. The interrupt handler of the processor then retrieves this data.

A UART control module was made for communication between the FPGA and a host computer so results could be displayed and further analyzed. This module takes the autocorrelation and analyzer output data sends them over a UART serial interface. An open-source UART module [53] was used to provide an 8-bit wide streaming interface and make the 3.125 megabaud UART communication port. A 4096-byte deep FIFO was used to buffer data to the UART interface. Our FPGA development board has a UART to USB module that then allows for direct connection to a PC. A Windows GUI application was created for control of the DCS system and display of the data output. This application allows for the input of the optical absorption coefficient (μ_a), reduced scattering coefficient (μ_s'), and the separation between source and detector fibers for a particular measurement. It then uses these values to determine constants used for the DCS analyzer fitting before sending them to the FPGA. The GUI software then plots the autocorrelation and analyzer outputs in real time as the FPGA generates them and saves the data to a file for further analysis.

2.4. System Evaluation and Comparison

Our DCS system was evaluated by comparing its output to a lab-standard reference DCS system widely used by the DCS community, which consists of a 4-channel hardware correlator (Flex01LQ-05, Correlator.com, Bridgewater, NJ) and a computer to perform software curve fitting to determine the BFI in post-processing as we have described in detail previously [20,54–56]. A BNC splitter was used to feed the APD output signal to both the reference system and our FPGA DCS device so that both systems received the same photon pulses with identical optical setups. Several tests were conducted to compare these systems including phantom measurements and cuff ischemia experiments. All of these tests used the same source-detector separation of 1 cm.

The first phantom test was with a solid optical tissue phantom made from silicone ($\mu_s' = 17.2 \text{ cm}^{-1}$; $\mu_a = 0.23 \text{ cm}^{-1}$). Since a solid phantom does not have any motion, we expected there to be near zero measured flow with this phantom and establish the lower limits of these DCS systems. Since this low flow corresponds with a correlation that decays late, we used our 120-channel correlator configuration to fully capture the decay of the correlation. For other experiments, an 80-channel configuration is sufficient and allows for faster fitting.

The liquid phantoms consist of light-scattering particles suspended within a liquid medium. Unlike solid phantoms, liquid phantoms have Brownian motion that can be measured with DCS. By varying the viscosity of the liquid, we can change the rate of this motion. We prepared our base liquid phantom with a 2% dilution of Intralipid (Fresenius Kabi, Uppsala, Sweden) ($\mu_s' = \sim 20 \text{ cm}^{-1}$) with 100 $\mu\text{L/L}$ of India ink (Speedball, Super Black India Ink 385460, Statesville, NC) ($\mu_a = \sim 0.14 \text{ cm}^{-1}$). We also made liquid phantoms with increased viscosities through the addition of methyl cellulose (The Candlemaker's Store, Methyl Cellulose (Non-FDA) SADMETC, Hamilton, OH). Methyl cellulose concentrations of 0%, 0.0625%, 0.5%, and 1% were chosen to show four distinct flow rates as the flow decreases exponentially with the concentration of methyl cellulose [57]. For these phantom tests, we collected 30 seconds of data for each phantom at a measurement rate of 1 Hz, i.e., the BFI was computed every second from one second of photon count data.

We also performed arm cuff ischemia experiments to show the application of our system for the real-time measurement of muscle blood flow in humans. While the subject was sitting in the full Fowler's position, a blood pressure cuff was placed around the bicep of the subject's arm. The subject's arm was placed on a table to allow for stable measurement and an optical probe was secured to the measurement site. The subject was asked to sit for several minutes to allow for the blood flow to stabilize. 10 seconds of baseline measurements were taken before inflating the blood pressure cuff

up to 200 mmHg to cut off blood flow. The pressure was held for 25 seconds before releasing it and the measurement lasted until the blood flow returned to baseline. This experiment was performed three times with different measurement rates. One with a measurement rate of 1 Hz at the forearm for both systems, another at the forearm with the FPGA system set to 50 Hz, and the last performed on the palm with the FPGA system set to 50 Hz. We did not use a higher measurement rate for the reference system because its fastest measurement rate is 1 Hz.

3. Results

3.1. Optical Phantom Tests

To validate the accuracy of our correlator module, we first compared the results from our FPGA correlator module to those from the reference hardware correlator, referred to as the reference here for short. This allows us to see how well the correlations match prior to the curve-fitting analysis and see the changes in the correlations with varying flow. For purposes of display, the 30 correlations collected over each 30-second measurement period were averaged together.

Correlations from the solid phantom test are shown in Figure 4. Since our FPGA correlator uses a different tau configuration than the reference correlator, the data points between each set of data do not exactly overlap with each other. However, the correlation data from the FPGA correlator matches well with the reference results such that both correlations decay at the same rate.

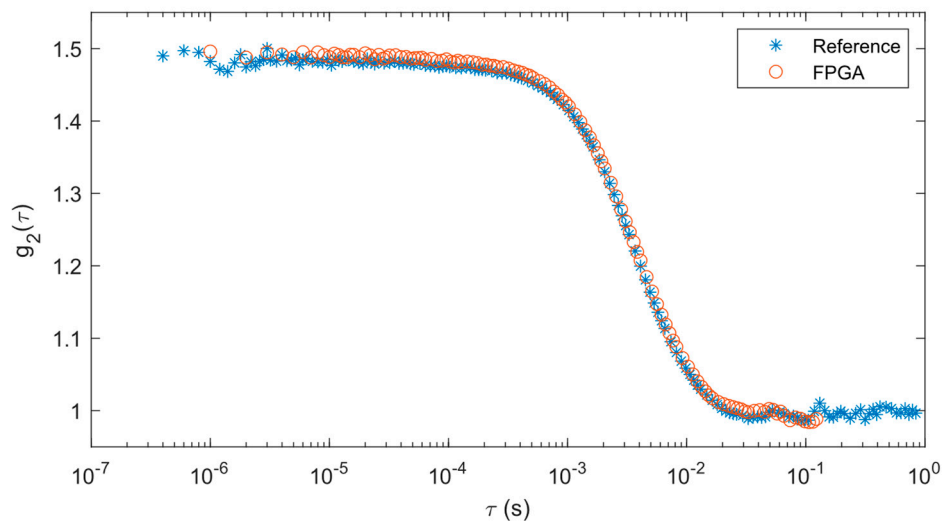


Figure 4. Correlations averaged over 30 seconds for solid phantom measurements for reference and FPGA correlators.

Results from curve fitting analysis provide a quantitative way of comparing these two approaches. The means and standard deviations of the BFIs derived from the curve fitting operations are shown in Table 1. It should be noted that the curve fitting done with the reference system and FPGA results are slightly different (~11%), most likely due to the differences in these algorithms. While the mean of the FPGA BFI is higher than the reference system, when considering the standard deviations, they are well within range of each other.

Table 1. Means and standard deviations of BFIs derived from 30 solid phantom correlations for reference and FPGA systems.

Data Source	Mean \pm Standard Deviation ($\times 10^{-11}$ cm ² /sec)
Reference	9.869 \pm 2.762
FPGA	10.961 \pm 2.956

We processed our liquid phantom results in the same way as the solid phantom. A comparison of the correlations between the two systems can be found in Figure 5. Blue markers represent the output from the reference correlator while brown markers are for FPGA data. Different marker shapes represent varying levels of methyl cellulose. The FPGA correlations remained consistent with the reference system results with each concentration of methyl cellulose. The correlation decay rates were slower as the methyl cellulose increased in concentration because it increased liquid viscosity.

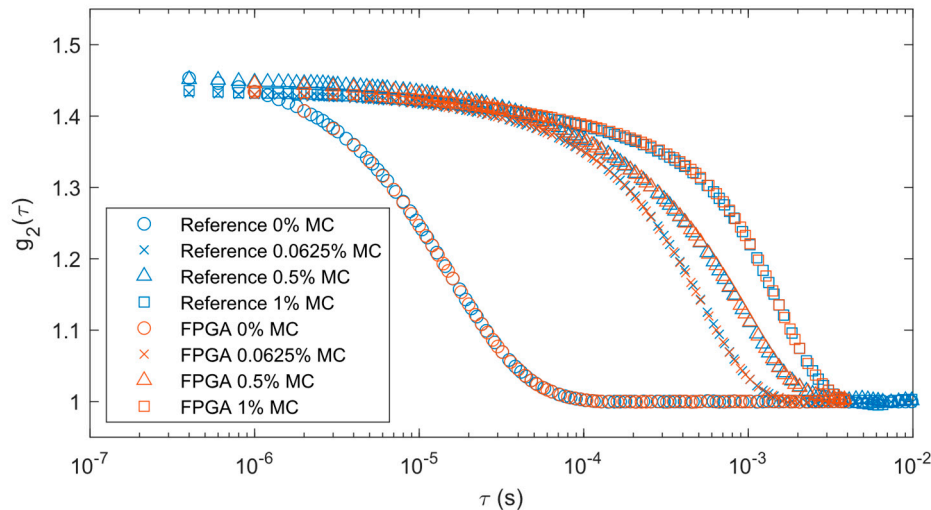


Figure 5. Correlations averaged over 30 seconds for liquid phantom measurements with varying levels of methyl cellulose (MC) for reference and FPGA correlators.

Curve fitting analysis results for the liquid phantoms are shown in Table 2. There is an expected decrease in mean flow as the concentration of methyl cellulose increases. The standard deviation of the measurements also decreases proportionally with the mean as the concentration increases.

Table 2. Means and standard deviations of BFIs derived from 30 liquid phantom correlations each from solutions of varying methyl cellulose concentrations for reference and FPGA systems.

Methyl Cellulose Concentration (%)	Data Source	Mean \pm Standard Deviation ($\times 10^{-11}$ cm ² /sec)
0.0625	Reference	12.548 \pm 2.1360
	FPGA	12.009 \pm 2.6367
0.5	Reference	8.2673 \pm 1.7543
	FPGA	7.6094 \pm 1.5856
1	Reference	4.1740 \pm 0.59629
	FPGA	3.8712 \pm 0.43825

3.2. Cuff Ischemia Tests

At the 1 Hz measurement rate, the BFI data from both systems match well across the experiment period when performed at the forearm, as shown in Figure 6. At the initial baseline, the flow for both systems are nearly identical with similar variations over time. As the cuff is inflated, the BFI decreases as expected until the cuff is released. At that point, the BFI rises suddenly due to reactive hyperemia. The data from the reference systems has some outliers where the BFI dips or spikes far from surrounding data points. A closer review of the relevant correlations found that poor fits caused these outliers.

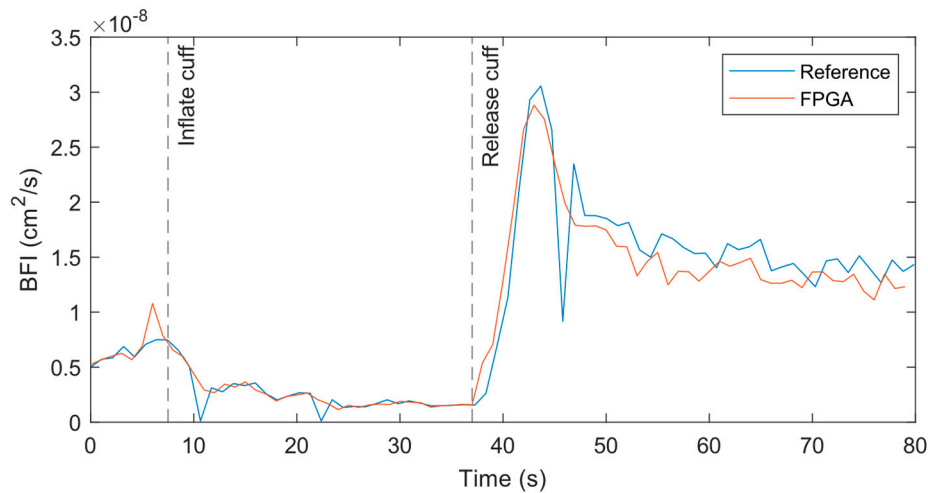


Figure 6. BFI from reference and FPGA in cuff ischemia experiment with both systems measuring at 1 Hz on the forearm with a source-detector separation of 1 cm.

To resolve the pulsatile flow in the BFI, we increased the measurement rate to 50 Hz for the FPGA system, while the hardware correlator-based reference system could only allow 1 Hz. The original 50 Hz output contains high frequency noise that makes it difficult to visualize the heartbeat and diastolic notch. However, with a simple 15-point moving average filter, we could obtain the data shown in Figure 7 indicating a clear pulsing in the BFI at a normal heart rate frequency. A wider, more aggressive filter could have been used, but at the cost of representing less accurately the amplitude of the pulsatile peaks. We are also able to observe the diastolic notch like previous work on fast DCS [58]. As with the prior 1 Hz measurement, the general trends in the BFI between the 50 Hz FPGA and 1 Hz reference measurements were nearly identical.

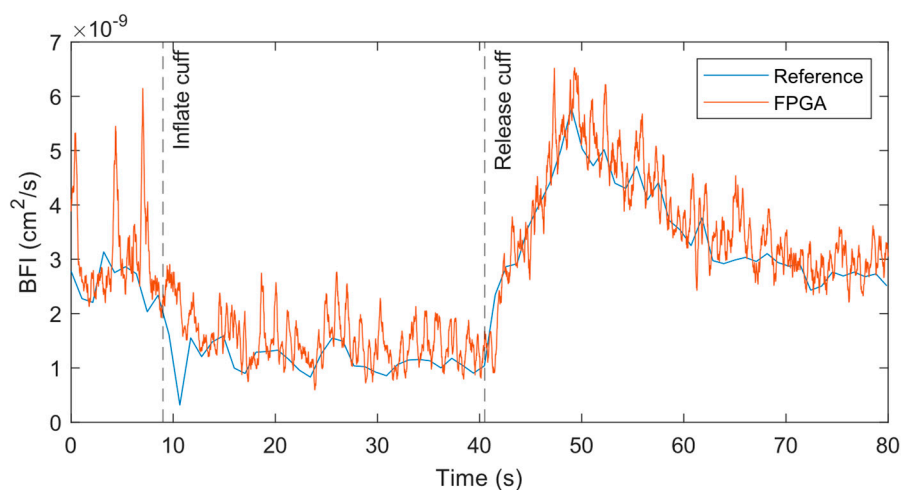


Figure 7. BFI from reference and FPGA in cuff ischemia experiment with reference measuring at 1 Hz and the FPGA at 50 Hz at the forearm with a source-detector separation of 1 cm. A 15-point moving average filter was applied to the FPGA data to remove high-frequency noise.

Next, Figure 8 shows the results from the experiment on the palm. We used a smaller 5-point moving average filter for this data since this data was less noisy than the forearm. The results showed a similar drop in BFI as the cuff is inflated (Figure 8a), but the pulsatile amplitude also decreased significantly during this period. Upon release of the cuff, the BFI increased and then came to baseline with time. The pulsatile flow quantified by the FPGA system was much more pronounced and the diastolic notch was clearly apparent (Figure 8b). Frequency spectrum data following the release of the

cuff indicated a peak at 1.45 Hz corresponds to the heart rate of the subject (Figure 8c). The other peaks correspond to the harmonics of the heart rate.

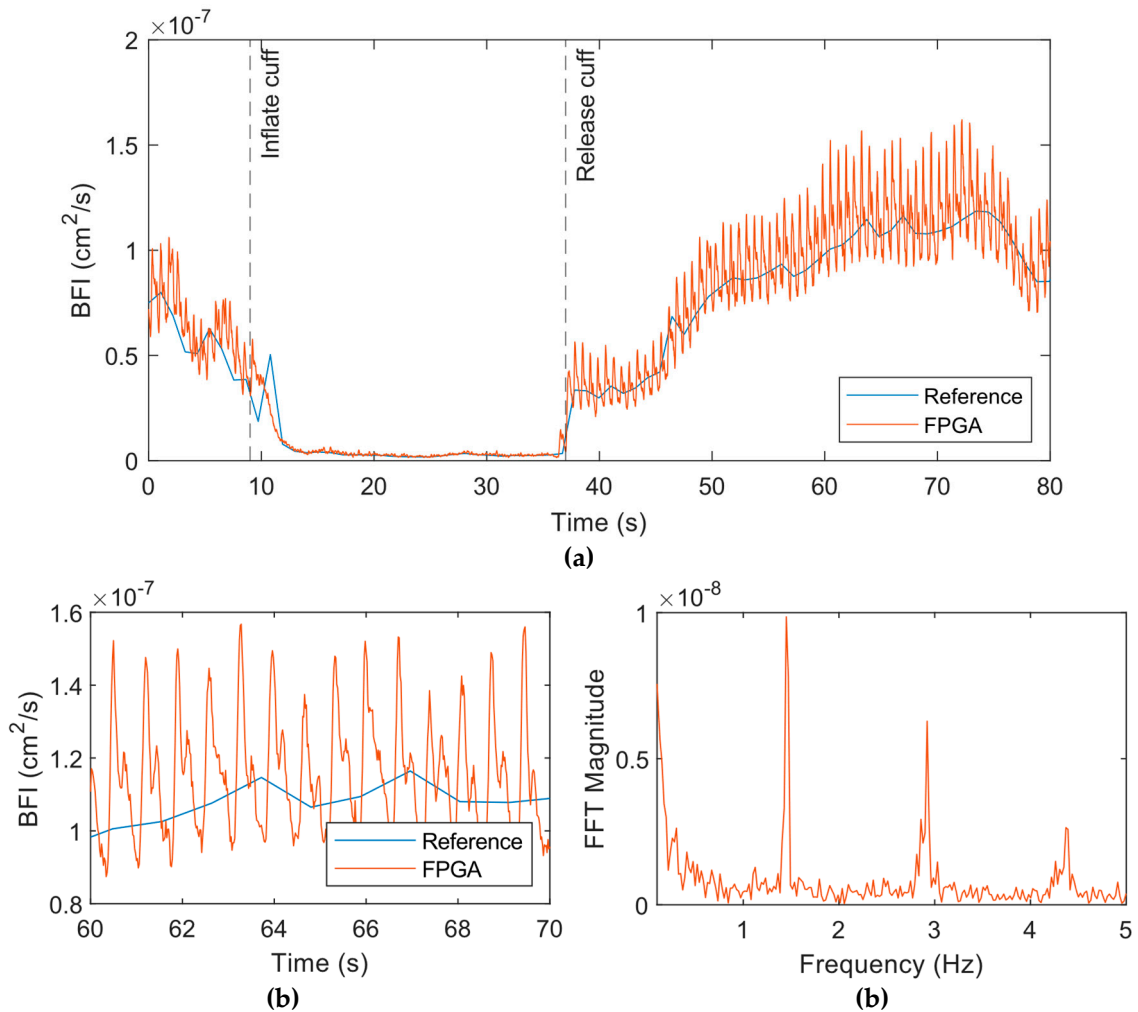


Figure 8. BFI from reference and FPGA in cuff ischemia experiment with reference measuring at 1 Hz and the FPGA at 50 Hz at the palm with a source-detector separation of 1 cm. A moving average filter with a window size of 5 data points was applied to the FPGA data to remove high-frequency noise. (a) Full time series from the experiment. (b) Zoomed in view of 10 seconds of time series data. The pulsatile flow and dirotic notch are clearly apparent here. (c) Frequency spectrum from an FFT of the FPGA BFI data following release of the cuff. The peak at 1.45 Hz corresponds to the heart rate of the subject.

4. Discussion

The FPGA implementation of a full DCS data processing system on a single chip shows the potential for making DCS more accessible for portable and wearable applications. Our FPGA implementation provides a complete device-on-chip solution for real-time DCS electronics from the direct output of an APD to the final BFI. With the integration of the correlator and analyzer modules on the same FPGA chip, we can achieve fast and accurate DCS analysis at a measurement rate of 50 Hz which is highly suitable for real-time applications. Our FPGA correlator can replace the function of expensive and inflexible hardware correlators with a customizable implementation tailored to specific physiological applications. Our FPGA analyzer can perform the curve fitting operation quickly, usually in approximately 150 μ s, which was confirmed by an embedded timer in the FPGA. This easily allows for real-time BFI analysis even at high measurement rates. There is no reliance on a high-performance computer for post-processing or the use of less accurate, simplified fitting procedures in software.

Our design is resource efficient as it uses only part of the relatively inexpensive and small FPGA on our development board. The whole design uses 15810 LUTs (25%), 19224 registers (15%), 15.5 block RAMs (11%), and 123 DSPs (51.25%) on an Artix-7 100T FPGA. The current single-channel implementation of our design shows only a fraction of the potential it has for enabling multi-channel, fast DCS measurements. Due to the immense speed at which our correlator and analyzer operate, we can fit more channels on our FPGA chip. In its current form, our correlator operates at a frequency of 100 MHz and can accept a new data point on every clock cycle. Our experiments used a photon counter binning size of 1 μ s for a single channel so a new data point is generated for the correlator at a rate of 1 MHz or once every 100 clock cycles. This leaves the correlator idle for the 99 remaining clock cycles. Instead of idling, we can use these clock cycles to perform correlations for other channels. This would theoretically allow for 100 channels to be correlated using the same correlator hardware. With an approximate average of 150 μ s per curve fit with our analyzer module, we can perform over 6000 fittings per second. For a DCS measurement rate of 50 Hz, one analyzer could process the data for up to 120 channels. Although the numbers are theoretical, they demonstrate the potential of our technology for use in a multi-channel, real-time DCS system.

A comparison of the results across our phantom and cuff ischemia experiments showed that our FPGA system was equivalent to the reference DCS system. A direct comparison of the correlations for each system shows matching results. BFI results coming out of our FPGA DCS analyzer show that our implementation is equivalent to the reference software curve fitting algorithms. The BFI data from the liquid phantom experiments showed that the BFI values from the FPGA system were slightly different than the reference system, possibly due to the small differences between the curve fitting of our FPGA and the software used for the reference system. For example, the FPGA system has 80 correlation values that are used for the curve fitting, while the reference system has 128, of which a segment of the correlation is selected for fitting. However, it should not affect the performance of the DCS system in practice as shown in the cuff ischemia test. Pulsatile flow could be resolved from our forearm cuff ischemia and palm measurements. We used a relatively short source-detector separation of 1 cm for all our experiments, which means we're measuring flow at a shallow depth. The highly vascularized and muscular area of the palm by the base of the thumb has more superficial flow than our forearm location which allows us to resolve much clearer pulsatile flow with the same equipment and signal-to-noise ratio.

Our approach has several limitations. Although the components of our design have flexible configurations and are easy to use, the post-processing software approach still offers a much more flexible solution for DCS research. Our analyzer implementation is fixed to the semi-infinite correlation diffusion equation, and it cannot be changed without major modifications to the FPGA logic. Changing any of the algorithms or models requires much more time than software code that can be easily updated. Additionally, our DCS analyzer uses the Nelder-Mead method to minimize the error between the measured and theoretical correlation. This method of minimization is much more practical to implement on an FPGA than gradient-based methods, but it can be susceptible to getting stuck at local minimums that generate suboptimal results. We largely eliminate this issue by providing an initial simplex to our analyzer that is in the expected range of the results and has had no observable issues with our methodology.

5. Conclusions

We have shown the development of a fully integrated DCS processing system that can perform all calculations necessary to produce a BFI from the output pulse of the photon detector on a single FPGA chip in real-time. We have validated our FPGA system against an existing lab standard DCS (reference) system and shown comparable results. Our system also has the capability to perform fast DCS measurements and can resolve pulsatile blood flow. Our future work will be to support multiple DCS channels with shared correlator and analyzer hardware. The development of this system can significantly lower the cost and footprint of the computational components of DCS and paves the way for portable, real-time DCS systems.

Author Contributions: Conceptualization, C. Moore. and W. Lin.; methodology, U. Sunar and W. Lin.; software, C. Moore.; validation, C. Moore, U. Sunar and W. Lin.; formal analysis, C. Moore; investigation, C. Moore, U. Sunar and W. Lin; resources, U. Sunar and W. Lin; data curation, C. Moore.; writing—original draft preparation, C. Moore; writing—review and editing, U. Sunar and W. Lin; visualization, U. Sunar and W. Lin; supervision, U. Sunar and W. Lin; project administration, U. Sunar and W. Lin; funding acquisition, U. Sunar. All authors have read and agreed to the published version of the manuscript.

Funding: This research was partially funded by an NIH R01 grant (NIBIB Brain Initiative 5R01EB031759-02).

Institutional Review Board Statement: Not applicable.

Informed Consent Statement: Not applicable.

Data Availability Statement: Not applicable.

Acknowledgments: The authors would like to acknowledge Sahar Sabaghian for her assistance with performing the cuff ischemia tests.

Conflicts of Interest: The authors declare no conflicts of interest.

References

1. E. M. Buckley, A. B. Parthasarathy, P. E. Grant, A. G. Yodh, and M. A. Franceschini, "Diffuse correlation spectroscopy for measurement of cerebral blood flow: future prospects," *Neurophotonics* (2014).
2. T. Durduran, R. Choe, W. B. Baker, and A. G. Yodh, "Diffuse optics for tissue monitoring and tomography," *Reports Prog. Phys.* (2010).
3. T. Durduran, A. G. Yodh, D. T., Y. A.G., T. Durduran, and A. G. Yodh, "Diffuse correlation spectroscopy for non-invasive, micro-vascular cerebral blood flow measurement," *Neuroimage* (2014).
4. R. C. Mesquita, T. Durduran, G. Yu, E. M. E. M. Buckley, M. N. M. N. Kim, C. Zhou, R. Choe, U. Sunar, and A. G. A. G. Yodh, "Direct measurement of tissue blood flow and metabolism with diffuse optics," *Philos. Trans. R. Soc. A Math. Phys. Eng. Sci.* **369**(1955), (2011).
5. D. T. and Y. A.G., "Diffuse correlation spectroscopy for non-invasive, micro-vascular cerebral blood flow measurement," *Neuroimage* (2014).
6. G. Yu, T. Durduran, C. Zhou, R. Cheng, and A. G. Yodh, "Near-infrared diffuse correlation spectroscopy for assessment of tissue blood flow," in *Handbook of Biomedical Optics* (2016).
7. T. Durduran, C. Zhou, E. M. Buckley, M. N. Kim, G. Yu, R. Choe, J. W. Gaynor, T. L. Spray, S. M. Durning, S. E. Mason, L. M. Montenegro, S. C. Nicolson, R. A. Zimmerman, M. E. Putt, J. Wang, J. H. Greenberg, J. A. Detre, A. G. Yodh, and D. J. Licht, "Optical measurement of cerebral hemodynamics and oxygen metabolism in neonates with congenital heart defects," *J. Biomed. Opt.* (2010).
8. G. Yu, T. F. Floyd, T. Durduran, C. Zhou, J. Wang, J. A. Detre, and A. G. Yodh, "Validation of diffuse correlation spectroscopy for muscle blood flow with concurrent arterial spin labeled perfusion MRI," *Opt. Express* (2007).
9. S. A. Carp, G. P. Dai, D. A. Boas, M. A. Franceschini, and Y. R. Kim, "Validation of diffuse correlation spectroscopy measurements of rodent cerebral blood flow with simultaneous arterial spin labeling MRI; towards MRI-optical continuous cerebral metabolic monitoring.," *Biomed. Opt. Express* (2), 553–565 (2010).
10. D. T., Z. C., B. E.M., K. M.N., Y. G., C. R., G. J.W., S. T.L., D. S.M., M. S.E., M. L.M., N. S.C., Z. R.A., P. M.E., W. J., G. J.H., D. J.A., Y. A.G., and L. D.J., "Optical measurement of cerebral hemodynamics and oxygen metabolism in neonates with congenital heart defects.," *J. Biomed. Opt.* (2010).
11. G. Yu, T. Durduran, C. Zhou, H. W. Wang, M. E. Putt, H. M. Saunders, C. M. Sehgal, E. Glatstein, A. G. Yodh, and T. M. Busch, "Noninvasive monitoring of murine tumor blood flow during and after photodynamic therapy provides early assessment of therapeutic efficacy," *Clin. Cancer Res.* (2005).
12. R. C. Mesquita, S. S. Schenkel, D. L. Minkoff, X. Lu, C. G. Favilla, P. M. Vora, D. R. Busch, M. Chandra, J. H. Greenberg, J. A. Detre, and A. G. Yodh, "Influence of probe pressure on the diffuse correlation spectroscopy blood flow signal: extra-cerebral contributions," *Biomed. Opt. Express* (2013).
13. F. C.G., M. R., K. M., G. J.H., D. J.A., Y. A.G., M. M.T., S. N., K. S.E., C. G. Favilla, R. Mesquita, M. Kim, J. H. Greenberg, J. A. Detre, A. G. Yodh, M. T. Mullen, N. Shafi, and S. E. Kasner, "Optical measurements of cerebral hemodynamics in acute cortical stroke," *Stroke* (2011).
14. A. B. Parthasarathy, W. B. Baker, K. Gannon, M. T. Mullen, J. A. Detre, and A. G. Yodh, "Clinical applications of high-speed blood flow measurements with diffuse correlation spectroscopy," in *Optical Tomography and Spectroscopy of Tissue XII* (2017).
15. A. B. Parthasarathy, K. P. Gannon, W. B. Baker, C. G. Favilla, R. Balu, S. E. Kasner, A. G. Yodh, J. A. Detre, and M. T. Mullen, "Dynamic autoregulation of cerebral blood flow measured non-invasively with fast diffuse correlation spectroscopy," *J. Cereb. Blood Flow Metab.* (2018).

16. G. Q. Yu, "Near-infrared diffuse correlation spectroscopy in cancer diagnosis and therapy monitoring," *J. Biomed. Opt.* (1), (2012).
17. W. B. Baker, R. Balu, L. He, V. C. Kavuri, D. R. Busch, O. Amendolia, F. Quattrone, S. Frangos, E. Maloney-Wilensky, K. Abramson, E. Mahanna Gabrielli, A. G. Yodh, and W. Andrew Kofke, "Continuous non-invasive optical monitoring of cerebral blood flow and oxidative metabolism after acute brain injury," *J. Cereb. Blood Flow Metab.* (2019).
18. R. M. Forti, C. G. Favilla, J. M. Cochran, W. B. Baker, J. A. Detre, S. E. Kasner, M. T. Mullen, S. R. Messé, W. A. Kofke, R. Balu, D. Kung, B. A. Pukenas, N. I. Sedora-Roman, R. W. Hurst, O. A. Choudhri, R. C. Mesquita, and A. G. Yodh, "Transcranial Optical Monitoring of Cerebral Hemodynamics in Acute Stroke Patients during Mechanical Thrombectomy," *J. Stroke Cerebrovasc. Dis.* (2019).
19. R. M. Forti, M. Katsurayama, J. Menko, L. Valler, A. Quiroga, A. L. E. Falcão, L. M. Li, and R. C. Mesquita, "Real-Time Non-invasive Assessment of Cerebral Hemodynamics With Diffuse Optical Spectroscopies in a Neuro Intensive Care Unit: An Observational Case Study," *Front. Med.* **7**, 147 (2020).
20. C. S. Poon, B. Rinehart, D. S. Langri, T. M. Rambo, A. J. Miller, B. Foreman, and U. Sunar, "Noninvasive optical monitoring of cerebral blood flow and eeg spectral responses after severe traumatic brain injury: A case report," *Brain Sci.* **11**(8), (2021).
21. S. A. Carp, D. Tamborini, D. Mazumder, K.-C. (Tony) Wu, M. R. Robinson, K. A. Stephens, O. Shatrovoy, N. Lue, N. Ozana, M. H. Blackwell, and M. A. Franceschini, "Diffuse correlation spectroscopy measurements of blood flow using 1064 nm light," *J. Biomed. Opt.* **25**(09), (2020).
22. L. Colombo, M. Pagliuzzi, S. Konugolu Venkata Sekar, D. Contini, T. Durduran, and A. Pifferi, "In vivo time-domain diffuse correlation spectroscopy above the water absorption peak," *Opt. Lett.* **45**(13), (2020).
23. M. T. Mullen, A. B. Parthasarathy, A. Zandieh, W. B. Baker, R. C. Mesquita, C. Loomis, J. Torres, W. Guo, C. G. Favilla, S. R. Messé, A. G. Yodh, J. A. Detre, S. E. Kasner, R. M. Forti, M. Katsurayama, J. Menko, L. Valler, A. Quiroga, A. L. E. Falcão, L. M. Li, R. C. Mesquita, A. A. Topjian, M. Fry, A. F. Jawad, S. T. Herman, V. M. Nadkarni, R. Ichord, R. A. Berg, D. J. Dlugos, N. S. Abend, M. Barud, W. Dabrowski, D. Siwicka-Gieroba, C. Robba, M. Bielacz, R. Badenes, C. S. Robertson, A. Kampfl, B. Pfausler, D. Denchev, H. P. Jaring, E. Schmutzhard, S. R. Leal-Noval, A. Cayuela, V. Arellano-Orden, A. Marín-Caballós, V. Padilla, C. Ferrándiz-Millón, Y. Corcia, C. García-Alfaro, R. Amaya-Villar, F. Murillo-Cabezas, S. B. Lewis, J. A. Myburgh, E. L. Thornton, P. L. Reilly, D. J. Davies, Z. Su, M. T. Clancy, S. J. E. Lucas, H. Dehghani, A. Logan, A. Belli, P. Esnault, H. Boret, A. Montcriol, E. Carre, B. Prunet, J. Bordes, P. Simon, C. Joubert, A. Dagain, E. Kaiser, E. Meaudre, A. K. Gupta, P. J. Hutchinson, P. Al-Rawi, S. Gupta, M. Swart, P. J. Kirkpatrick, D. K. Menon, A. K. Datta, M. Oddo, J. M. Levine, L. MacKenzie, S. Frangos, F. Feihl, S. E. Kasner, M. Katsnelson, B. Pukenas, E. MacMurtrie, E. Maloney-Wilensky, W. A. Kofke, P. D. Leroux, A. M. Spiotta, M. F. Stiefel, V. H. Gracias, A. M. Garuffe, W. A. Kofke, E. Maloney-Wilensky, A. B. Troxel, J. M. Levine, P. D. Le Roux, L. Colombo, M. Pagliuzzi, S. Konugolu Venkata Sekar, D. Contini, T. Durduran, and A. Pifferi, "Detection of Electrographic Seizures by Critical Care Providers Using Color Density Spectral Array after Cardiac Arrest Is Feasible," *Front. Med.* **16**(5), 147 (2015).
24. T. Durduran, A. G. Yodh, D. T., and Y. A.G., "Diffuse correlation spectroscopy for non-invasive, microvascular cerebral blood flow measurement," *Neuroimage* (2014).
25. M. T. Mullen, A. B. Parthasarathy, A. Zandieh, W. B. Baker, R. C. Mesquita, C. Loomis, J. Torres, W. Guo, C. G. Favilla, S. R. Messé, A. G. Yodh, J. A. Detre, and S. E. Kasner, "Cerebral Blood Flow Response During Bolus Normal Saline Infusion After Ischemic Stroke," *J. Stroke Cerebrovasc. Dis.* **28**(11), (2019).
26. M. N. Kim, B. L. Edlow, T. Durduran, S. Frangos, R. C. Mesquita, J. M. Levine, J. H. Greenberg, A. G. Yodh, and J. A. Detre, "Continuous optical monitoring of cerebral hemodynamics during head-of-bed manipulation in brain-injured adults," *Neurocrit. Care* (2014).
27. D. R. Busch, R. Balu, W. B. Baker, W. Guo, L. He, M. Diop, D. Milej, V. Kavuri, O. Amendolia, K. St. Lawrence, A. G. Yodh, and W. A. Kofke, "Detection of Brain Hypoxia Based on Noninvasive Optical Monitoring of Cerebral Blood Flow with Diffuse Correlation Spectroscopy," *Neurocrit. Care* (2019).
28. J. Selb, K.-C. Wu, J. Sutin, P.-Y. (Ivy) Lin, P. Farzam, S. Bechek, and A. Shenoy, "Prolonged monitoring of cerebral blood flow and autoregulation with diffuse correlation spectroscopy in neurocritical care patients," *Neurophotonics* **5**(04), (2018).
29. C. Zhou, R. Choe, N. Shah, T. Durduran, G. Yu, A. Durkin, D. Hsiang, R. Mehta, J. Butler, A. Cerussi, B. J. Tromberg, and A. G. Yodh, "Diffuse optical monitoring of blood flow and oxygenation in human breast cancer during early stages of neoadjuvant chemotherapy," *J. Biomed. Opt.* (2007).
30. R. Choe, M. E. Putt, P. M. Carlile, T. Durduran, J. M. Giammarco, D. R. Busch, K. W. Jung, B. J. Czerniecki, J. Tchou, M. D. Feldman, C. Mies, M. A. Rosen, M. D. Schnall, A. DeMichele, and A. G. Yodh, "Optically measured microvascular blood flow contrast of malignant breast tumors," *PLoS One* (2014).
31. U. Sunar, D. Rohrbach, N. Rigual, E. Tracy, K. Keymel, M. T. Cooper, H. Baumann, and B. H. Henderson, "Monitoring photobleaching and hemodynamic responses to HPPH-mediated photodynamic therapy of head and neck cancer: a case report," *Opt. Express* **18**(14), 14969 (2010).

32. U. Sunar, S. Makonnen, C. Zhou, T. Durduran, G. Yu, H.-W. Wang, W. M. F. Lee, and A. G. Yodh, "Hemodynamic responses to antivasular therapy and ionizing radiation assessed by diffuse optical spectroscopies," *Opt. Express* **15**(23), (2007).
33. U. Sunar, "Monitoring photodynamic therapy of head and neck malignancies with optical spectroscopies," *World J Clin Cases* **1**(3), 96–105 (2013).
34. U. Sunar, S. Makonnen, H. W. Wang, T. Durduran, C. Zhou, G. Yu, W. M. F. Lee, and A. G. Yodh, "Non-invasive, continuous monitoring of a vascular targeting drug by diffuse optical blood flow and blood oxygenation measurements," in *Optics InfoBase Conference Papers* (2006).
35. H. S. Yazdi, T. D. O'Sullivan, A. Leproux, B. Hill, A. Durkin, S. Telep, J. Lam, S. S. Yazdi, A. M. Police, R. M. Carroll, F. J. Combs, T. Strömberg, A. G. Yodh, and B. J. Tromberg, "Mapping breast cancer blood flow index, composition, and metabolism in a human subject using combined diffuse optical spectroscopic imaging and diffuse correlation spectroscopy," *J. Biomed. Opt.* (2017).
36. J. M. Cochran, S. H. Chung, A. Leproux, W. B. Baker, D. R. Busch, A. M. Demichele, J. Tchou, B. J. Tromberg, and A. G. Yodh, "Longitudinal optical monitoring of blood flow in breast tumors during neoadjuvant chemotherapy," *Phys. Med. Biol.* (2017).
37. S. H. Chung, M. D. Feldman, D. Martinez, H. Kim, M. E. Putt, D. R. Busch, J. Tchou, B. J. Czerniecki, M. D. Schnall, M. A. Rosen, A. DeMichele, A. G. Yodh, and R. Choe, "Macroscopic optical physiological parameters correlate with microscopic proliferation and vessel area breast cancer signatures," *Breast Cancer Res.* (2015).
38. D. R. Busch, R. Choe, T. Durduran, L. Chaby, M. A. Rosen, and A. G. Yodh, "Measurement of micro-vascular blood flow in the human breast during compression with diffuse correlation spectroscopy," in *Photonics West BIOS* (2009).
39. D. A. Boas, L. E. Campbell, and A. G. Yodh, "Scattering and imaging with diffusing temporal field correlations," *Phys. Rev. Lett.* (1995).
40. D. A. Boas and A. G. Yodh, "Spatially varying dynamical properties of turbid media probed with diffusing temporal light correlation," *J. Opt. Soc. Am. A* (1997).
41. D. Wang, A. B. Parthasarathy, W. B. Baker, K. Gannon, V. Kavuri, T. Ko, S. Schenkel, Z. Li, Z. Li, M. T. Mullen, J. A. Detre, and A. G. Yodh, "Fast blood flow monitoring in deep tissues with real-time software correlators," *Biomed. Opt. Express* **7**(3), (2016).
42. J. Dong, R. Bi, J. H. Ho, P. S. P. Thong, K.-C. Soo, and K. Lee, "Diffuse correlation spectroscopy with a fast Fourier transform-based software autocorrelator," *J. Biomed. Opt.* **17**(9), 97004 (2012).
43. T. M. Uner, K. R. Cowdrick, R. O. Brothers, T. Boodooram, H. Zhao, V. Goyal, E. Sathialingam, A. Quadri, K. Turrentine, M. M. Akbar, S. E. Triplett, S. Bai, and E. M. Buckley, "Normative cerebral microvascular blood flow waveform morphology assessed with diffuse correlation spectroscopy," *Biomed. Opt. Express* **14**(7), 3635–3653 (2023).
44. C. H. Moore and W. Lin, "FPGA Correlator for Applications in Embedded Smart Devices," *Biosensors* **12**(4), 236 (2022).
45. W. Lin, D. R. Busch, C. C. Goh, J. Barsi, and T. F. Floyd, "Diffuse Correlation Spectroscopy Analysis Implemented on a Field Programmable Gate Array," *IEEE Access* **7**, 122503–122512 (2019).
46. M. Asif, X. Guo, A. Hu, and J. Miao, "An FPGA-Based 1-GHz, 128 x 128 Cross-Correlator for Aperture Synthesis Imaging," *IEEE Trans. Very Large Scale Integr. Syst.* **28**(1), 129–141 (2020).
47. M. Asif, X. Guo, J. Zhang, and J. Miao, "An FPGA based 1.6 GHz cross-correlator for synthetic aperture interferometric radiometer," in *2017 Progress in Electromagnetics Research Symposium - Fall (PIERS - FALL)* (IEEE, 2017).
48. J. Buchholz, J. W. Krieger, G. Mocsar, B. Kreith, E. Charbon, G. Vamosi, U. Keschull, and J. Langowski, "FPGA implementation of a 32x32 autocorrelator array for analysis of fast image series," *Opt Express* **20**(16), 17767–17782 (2012).
49. A. Islambek, K. Yang, W. Li, and K. Li, "FPGA-based real-time autocorrelator and its application in dynamic light scattering," *Optik (Stuttg.)* **194**, 163047 (2019).
50. J. A. Nelder and R. Mead, "A Simplex Method for Function Minimization," *Comput. J.* **7**(4), 308–313 (1965).
51. W. Liu, J. Shen, and X. Sun, "Design of Multiple-Tau Photon Correlation System Implemented by FPGA," in *2008 International Conference on Embedded Software and Systems* (IEEE, 2008).
52. J. Mathews and K. Fink, "Numerical Methods Using Matlab, 4th Edition," in (Prentice-Hall Inc., 2004), pp. 430–436.
53. J. Cabal, "Simple UART for FPGA," (2021).
54. B. Rinehart, C. S. Poon, and U. Sunar, "Quantification of perfusion and metabolism in an autism mouse model assessed by diffuse correlation spectroscopy and near-infrared spectroscopy," *J. Biophotonics* **14**(11), (2021).
55. J. Li, C. S. Poon, J. Kress, D. J. Rohrbach, and U. Sunar, "Resting-state functional connectivity measured by diffuse correlation spectroscopy," *J. Biophotonics* (2018).

56. C.-S. Poon, F. Long, and U. Sunar, "Deep learning model for ultrafast quantification of blood flow in diffuse correlation spectroscopy," *Biomed. Opt. Express* **11**(10), 5557 (2020).
57. L. Cortese, G. Lo Presti, M. Pagliazzi, D. Contini, A. Dalla Mora, A. Pifferi, S. Konugolu Venkata Sekar, L. Spinelli, P. Taroni, M. Zanoletti, U. Weigel, and T. Durduran, "A recipe for near infrared spectroscopy and diffuse correlation spectroscopy phantoms with tunable optical and dynamic properties," in *Optics InfoBase Conference Papers* (2018).
58. D. Wang, A. B. Parthasarathy, W. B. Baker, K. Gannon, V. Kavuri, T. Ko, S. Schenkel, Z. Z. Li, Z. Z. Li, M. T. Mullen, J. A. Detre, and A. G. Yodh, "Fast blood flow monitoring in deep tissues with real-time software correlators," *Biomed. Opt. Express* (2016).

Disclaimer/Publisher's Note: The statements, opinions and data contained in all publications are solely those of the individual author(s) and contributor(s) and not of MDPI and/or the editor(s). MDPI and/or the editor(s) disclaim responsibility for any injury to people or property resulting from any ideas, methods, instructions or products referred to in the content.